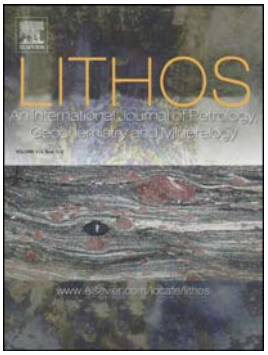

Origin of the late Early Cretaceous granodiorite and associated dioritic dikes in the Hongqilafu pluton, northwestern Tibetan Plateau: A case for crust–mantle interaction

Jiyong Li, Yaoling Niu, Yan Hu, Shuo Chen, Yu Zhang, Meng Duan, Pu Sun

PII: S0024-4937(16)30114-1
DOI: doi: 10.1016/j.lithos.2016.05.028
Reference: LITHOS 3947

To appear in: *LITHOS*

Received date: 23 February 2016
Accepted date: 31 May 2016

Please cite this article as: Li, Jiyong, Niu, Yaoling, Hu, Yan, Chen, Shuo, Zhang, Yu, Duan, Meng, Sun, Pu, Origin of the late Early Cretaceous granodiorite and associated dioritic dikes in the Hongqilafu pluton, northwestern Tibetan Plateau: A case for crust–mantle interaction, *LITHOS* (2016), doi: 10.1016/j.lithos.2016.05.028

Origin of the late Early Cretaceous granodiorite and associated dioritic dikes in the Hongqilafu pluton, northwestern Tibetan Plateau: A case for crust-mantle interaction

Jiyong Li [a, b, c*], Yaoling Niu [a, b, d*], Yan Hu [a, b, c], Shuo Chen [a, b, c], Yu Zhang [e], Meng Duan [f], Pu Sun [a, b, c]

[a] Institute of Oceanology, Chinese Academy of Sciences, Qingdao 266071, China

[b] Laboratory for Marine Geology, Qingdao National Laboratory for Marine Science and Technology, Qingdao 266061, China

[c] University of Chinese Academy of Sciences, Beijing 100049, China

[d] Department of Earth Sciences, Durham University, Durham DH1 3LE, UK

[e] School of Earth Science, Lanzhou University, Lanzhou 730000, China

[f] School of Earth Science and Resources, China University of Geosciences, Beijing 100083, China

[*]Corresponding authors:

Mr. Jiyong Li (lijiy09@163.com)

Professor Yaoling Niu (yaoling.niu@foxmail.com)

Current address:

Institute of Oceanology

Chinese Academy of Sciences

No. 7 Nanhai Road, Qingdao 266071, China

Phone and Fax: +86 0532 82898980

Abstract

We present a detailed study of geochronology, mineral chemistries, bulk-rock major and trace element abundances, and Sr-Nd-Hf isotope compositions of the granodiorite and associated dioritic dikes in the Hongqilafu pluton at the northwestern margin of the Tibetan Plateau. The granodiorite and dioritic dikes yielded zircon U-Pb ages of ~104 Ma and ~100 Ma, respectively. The dioritic dikes comprise varying lithologies of gabbroic diorite, diorite porphyry and granodiorite porphyry, exhibiting a compositional spectrum from intermediate to felsic rocks. Their mineral compositions display disequilibrium features such as large major element compositional variations of plagioclase, clinopyroxene and amphibole crystals. These dioritic dikes are enriched in incompatible elements (Ba, Rb, Th, U, K) and Sr-Nd-Hf isotopes ($^{87}Sr/^{86}Sr_i$: 0.7066 to 0.7071, $\varepsilon_{Nd}(t)$: -5.3 to -7.4, $\varepsilon_{Hf}(t)$: -3.6 to -6.2). We suggest that the dioritic dikes were most likely derived from partial melting of mantle wedge metasomatized by the subducted/subducting seafloor with a sediment component, followed by AFC processes with fractional crystallization of clinopyroxene, amphibole and plagioclase and assimilation of lower continental crust. The mantle-wedge derived magma parental to the dioritic dikes underplated and induced the lower continental crust to melt, forming the felsic crustal magma parental to the granodiorite with mantle melt signatures and having more enriched isotope compositions ($^{87}Sr/^{86}Sr_i$: 0.7087 to 0.7125, $\varepsilon_{Nd}(t)$: -9.5 to -11.6, $\varepsilon_{Hf}(t)$: -10.3 to -14.1) than those of the dioritic dikes. The Hongqilafu pluton is thus the product of mantle-crust interaction at an active continental margin subduction setting over the period of several million years. This understanding further indicates that the closure timing of the Shyok back-arc basin and the collision between the Kohistan-Ladakh Arc and the Karakoram Terrane may have taken place later than ~100 Ma.

Keywords: late Early Cretaceous; dioritic dikes; granodiorite; crust-mantle interaction; northwestern Tibetan Plateau

1 Introduction

The continental crust is generally interpreted to have formed as a result of melt extraction from the Primitive Mantle in Earth's early history and grown gradually to the present-day size (Hofmann, 1988) although different models exist with varying details (Allègre and Rousseau, 1984; Armstrong and Harmon, 1981; Collerson and Kamber, 1999; Taylor and McLennan, 1995). As an inevitable process during crust accretion-related magmatism, crust-mantle interaction has been the subject of much research. Models have been proposed to characterize crust-mantle interaction such as "underplating", "delamination", "convective removal", "tectonic erosion" (Bergantz, 1989; Clift et al., 2009; Conrad and Molnar, 1997; Kay and Kay, 1993; Lee, 2012; Lee and Anderson, 2015). All these are probable processes, but details of these processes need better understanding. As one of the principal constituents of continental crust, granites and granitoids must retain the messages on the perceived crust-mantle interaction (Chen et al., 2009; Wu et al., 2012; Xia et al., 2014; Yang et al., 2007). Revealing such messages therein will facilitate elucidating the processes of continental crust growth and evolution.

The India-Asia continental collision and convergence since the Early Cenozoic has resulted in the largest uplift structure on the Earth, i.e., the Greater Tibetan Plateau (Bouilhol et al., 2013; Mo et al., 2007, 2008; Yin et al., 1999). Previously, the Greater Tibetan Plateau had experienced long-term amalgamation and orogeny of several continental collision events since the Early Paleozoic (Niu et al., 2013; Zhu et al.,

2013). However, the pre-Cenozoic geological evolution of the northwestern Tibetan Plateau remains unclear and further studies are in urgent need. Extensive magmatism and associated granitoids therein have not yet well been recognized because of the difficult access at the high altitude and because of lacking precise dating and geochemical data on the available samples.

In this paper, we focus on the tectonically important yet poorly studied Hongqilafu pluton at the northwestern margin of the Tibetan Plateau (Fig. 1a). Up to now, only one study (Jiang et al., 2014) noted the Hongqilafu pluton which consists of metaluminous high-K calc-alkaline granodiorite and yielded zircon U-Pb age of 102.2 ± 1.4 Ma. Jiang et al. (2014) suggested that the granodiorite in the Hongqilafu pluton was generated by crystal fractionation of basaltic magmas in a continental arc setting without even mentioning the dioritic dikes that intruded the granodiorite (Fig. 2). In this study, we emphasize the geological and petrogenetic significance of these dikes in order to better understand the petrogenesis of the Hongqilafu pluton.

We present age data, major and trace elements analyses and Sr-Nd-Hf isotope compositions of the granodiorite and associated dioritic dikes in the Hongqilafu pluton to place constraints on their petrogenesis and to elucidate crust-mantle interaction in the context of the tectonic evolution of the Greater Tibetan Plateau.

2 Geological background

The northwestern Tibetan Plateau adjoins the Tarim Basin to the north and the Himalaya to the south, extending from the Altyn Tagh Fault and the Eastern Kunlun Orogen in the east to the Pamir Plateau in the west. It is offset by the Miocene dextral Karakoram Fault (KF) (Bhutani et al., 2003) (Fig. 1a).

To the east of the KF, several terranes and suture zones from north to south have

been recognized (Fig. 1a): (1) the North Kunlun Terrane (NKT); (2) the Oytag-Kudi-Qimanyute Suture (OKS); (3) the Sorth Kunlun Terrane (SKT); (4) the Mazha-Kangxiwa-Anyemaqen Suture (MKS); (5) the Tashkurghan-Tianshuihai Terrane (TST); (6) the Hongshanhu-Qiaoertianshan-Jinshajiang Suture (HQS); (7) the Qiangtang Terrane (QTT); (8) the Bangonghu-Nujiang Suture (BNS). The geological details can be found in the recent literatures (Cao et al., 2015; Hu et al., 2015; Jiang et al., 2008; Wang et al., 2002; Xiao et al., 2005; Zhang et al., 2016), especially the 1:1,500,000 Geological Map Series (Pan et al., 2004).

To the west of the KF are, from north to south, the following tectonic units (Fig. 1a):

The Karakoram Terrane (KT), assumed to be the western extension of the Lhasa Terrane in Tibet, is bounded by the Tirich Mir Fault (TMF) from the South Pamir Terrane to the north and by the Shyok Suture Zone (SSZ) from the Kohistan-Ladakh Arc (KLA) to the south (Zanchi and Gaetani, 2011). It mainly consists of highly deformed and metamorphosed sedimentary rocks including Precambrian basement overlain by Paleozoic and Mesozoic sedimentary covers in the northern KT and metamorphic belt in the southern KT (Fraser et al., 2001; Searle et al., 2010; Zanchi and Gaetani, 2011), which has been interpreted to have affinity with Gondwana (Gaetani, 1997; Heuberger et al., 2007). In addition, the Karakoram Batholith comprises the largest intrusive bodies such as the Cretaceous calc-alkaline granitoids (plus andesites) and the Miocene two-mica leucogranites (Ravikant et al., 2009).

The Shyok Suture Zone (SSZ), an important boundary between the Karakoram Terrane (KT) and the Kohistan-Ladakh Arc (KLA) - back arc system (Thakur and Misra, 1984), is made up of Cretaceous volcanic-sedimentary formations intruded by granodioritic plutons (Rolland et al., 2000). However, the closure timing of Shyok

basin is still controversial (see below) (Clift et al., 2002; Heuberger et al., 2007).

The Kohistan-Ladakh Arc (KLA), located between the Shyok Suture Zone (SSZ) and the Indus-Tsangpo Suture Zone (ITSZ), is interpreted as a Mesozoic intra-oceanic volcanic arc in response to the north-dipping subduction of the Neo-Tethyan oceanic crust beneath the KLA. The initiation of this subduction is interpreted as being indicated by the ~154 Ma calc-alkaline Matum Das intrusion (Schaltegger et al., 2003). The KLA comprises arc-related volcanic rocks, metamorphic rocks and volcaniclastic sediments (Burg, 2011; Coward et al., 1987). Meanwhile, the exposed Kohistan-Ladakh batholith shows two intrusive episodes of (1) the 103-83 Ma mafic-ultramafic rocks and arc-related volcanic rocks and (2) the 67-50 Ma diorite-granodiorite-granite (Ravikant et al., 2009).

The Hongqilafu pluton, one of the plutons of the Karakoram batholith, is located in the eastern segment of the KT, and intruded the lower Permian siltstone and slate sedimentary strata (Fig. 1b). Besides, the dioritic dikes intruded the granodiorite, whose chilled margins developed at the contact with the granodiorite are also observed (Fig. 2).

3 Analytical methods

In this study, we selected 2 samples (dioritic dike sample XKL12-21 and granodiorite sample XKL12-31) for zircon U-Pb dating and 9 samples (4 dioritic dike and 5 granodiorite samples) for whole-rock major and trace elements analysis. In addition, 6 samples (3 dioritic dike and 3 granodiorite samples) were analyzed for whole-rock Sr-Nd-Hf isotope compositions. Some principal mineral phases (e.g., clinopyroxene, plagioclase, amphibole and biotite) have been analyzed for major element compositions using electron microprobe analyzer (EPMA).

3.1 Zircon U-Pb isotopic dating

Zircon separation was done using combined methods of heavy liquid and magnetic extraction plus hand-picking under a binocular in the Langfang Institute of Regional Geological Survey in China. The selected zircon grains were mounted in an epoxy resin disk and polished to expose the interior for imaging and analysis. All the polished zircon grains were examined using cathodoluminescence (CL) images prior to the U-Pb analysis at China University of Geosciences in Wuhan (CUGW). Zircon U-Pb dating was done using a laser ablation inductively coupled plasma mass spectrometer (LA-ICP-MS) at CUGW. Zircon 91500 was analyzed twice between every five unknown analyses as the external standard for U-Pb dating. Trace element compositions of zircons were calibrated against multiple-reference materials (BCR-2G and BIR-1G) as external standards in combination with Si^{29} as internal standard. Our analysis follows the procedure by Liu et al. (2010a, b) with the data reduction done using ICPMSDataCal (ver. 8.0) (Liu et al., 2010a, b). The weighted mean age calculations and concordia diagrams were done using isoplot/Exversion 4.15 (Ludwig, 2012).

3.2 Mineral compositions analysis

Mineral analysis was carried out using a JXA-8100 microprobe at Chang'an University, China. The operating conditions were a 15 kV accelerating potential with a probe current of 10 nA and the electron beam diameter of 1 μm, 10s counting time and ZAF correction procedure for data reduction. The detection limits of measured oxides were less than 0.01%. The error was lower than 5%.

3.3 Whole-rock major and trace elements analysis

The whole-rock major and trace elements analysis was done at China University of Geosciences in Beijing (CUGB), using Leeman Prodigy inductively coupled plasma-optical emission spectroscopy (ICP-OES) and Agilent-7500a inductively coupled plasma mass spectrometry (ICP-MS), respectively. The analytical uncertainties are generally less than 1% for most major elements with the exception of TiO_2 (~1.5%) and P_2O_5 (~2%). The loss on ignition was measured by placing 1 g of sample powder in the furnace at 1000℃ for several hours before cooled in a desiccator and reweighted. The Analytical details are given in Song et al. (2010).

3.4 Sr-Nd-Hf isotopes analysis

The Sr-Nd-Hf isotopes analysis was done using a Micromass Isoprobe multi-collector inductively coupled plasma mass spectrometer (MC-ICP-MS) at Guangzhou Institute of Geochemistry, Chinese Academy of Sciences (GIG-CAS). For whole-rock Sr-Nd isotopes analysis, rock powders were dissolved with HF-HNO_3 mixtures, using analytical procedures described by Ma et al. (2013a, b). Additionally, 100 mg rock powder and 200 mg $Li_2B_4O_7$ were mixed homogeneously for Hf purification, following the methods described by Li et al. (2006). All measured $^{87}Sr/^{86}Sr$, $^{143}Nd/^{144}Nd$ and $^{176}Hf/^{177}Hf$ ratios were normalized to $^{86}Sr/^{88}Sr = 0.1194$, $^{146}Nd/^{144}Nd = 0.7219$ and $^{179}Hf/^{177}Hf = 0.7325$, respectively. During the course of this study, analyses of NBS987 standard gave $^{87}Sr/^{86}Sr = 0.710247 \pm 0.000008$ (n = 12, 2σ). The $^{143}Nd/^{144}Nd$ ratios of the standard Jndi-1 and the $^{176}Hf/^{177}Hf$ ratios of the standard JMC14374 were 0.512093 ± 0.000004 (n = 17, 2σ) and 0.282180 ± 0.000004 (n = 17, 2σ), respectively. The Sr-Nd-Hf isotopes of USGS reference material

BHVO-2 gave 0.703474 ± 0.000008 (2σ), 0.512954 ± 0.000005 (2σ) and 0.283073 ± 0.000004 (2σ) respectively, within the analytical error of the recommended values (GeoREM, http://georem.mpch-mainz.gwdg.de/).

4 Petrography and mineral compositions

The sample details in the Hongqilafu pluton are given in Appendix 1. Microprobe analyses of clinopyroxene, amphibole, plagioclase, and biotite for dioritic dike and granodiorite samples are given in Appendix 2, in which Fe^{2+} and Fe^{3+} values of amphibole were re-calculated after Lin and Peng (1994).

4.1 Dioritic dikes

The dioritic dikes comprise several rock types, including gabbroic diorite, diorite to granodiorite with porphyritic textures. The phenocrysts are clinopyroxene, amphibole, biotite and plagioclase with the groundmass having the same mineralogy, but finer-grain size (Fig. 3; Fig. S1).

There are some disequilibrium textures in gabbroic diorite (XKL12-21): (1) all clinopyroxene crystals show large compositional variations in MgO (11.50 - 16.57 wt%), TFeO (total Fe) (6.24 - 13.02 wt%) and Cr_2O_3 (0 - 0.99 wt%) (Fig. 3a, b; Fig. 6a, b), plotting in the augite and salite fields in the $CaSiO_3$-$MgSiO_3$-$FeSiO_3$ diagram (Fig. 5c); (2) some clinopyroxene phenocrysts have melt corrosion/absorption features with replacement by small grains of biotite and plagioclase (Fig. S1h); (3) the plagioclase phenocrysts in single thin sections have highly variable compositions (e.g., high An_{65-82} and low An_{41-48}; Fig. 3c, d); (4) the small plagioclase grains in the groundmass also show large compositional variation (An_{38-67}; Fig. 5a).

Amphibole crystals in all dioritic dike samples mainly plot in the pargasite field

(Fig. 5d) with variable $Mg^{\#}$ (0.48 - 0.79) ($Mg^{\#}$ = Mg/[Mg+Fe^{2+}]) (Appendix 2). In diorite sample XKL12-25, some amphibole crystals exhibit obvious disequilibrium features with multiple and reverse zoning with plagioclase and K-feldspar inclusions (Fig. 3e, f), suggesting that the magma system parental to the dioritic dikes was in an open environment. The amphibole crystals gradually growing around the nucleus of plagioclase or K-feldspar indicates the replenishment of new and more primitive basic magma during magma evolution. Besides, the compositions of plagioclase phenocrysts in other dioritic dike samples also exhibit large variations in the core, mantle and rim of phenocrysts (Fig. 5a).

4.2 Granodiorite

The granodiorite samples have medium-coarse grained granular textures and contain plagioclase (~35 - 40%), biotite (~15 - 20%), quartz (~30 - 35%), K-feldspar (~5 - 10%) (Fig. 4) and accessory minerals such as allanite, zircon and Fe-Ti oxides, except for sample XKL12-29 that has porphyritic texture with plagioclase and quartz phenocrysts and fine-grained quartz and plagioclase in the groundmass (Fig. 4c; Fig. S2). Overall, the plagioclase crystals are euhedral to subhedral and have varying compositions (An_{11-57}) in different analytical spots (rim, mantle or core of plagioclase) for the granodiorite samples (Fig. 5b). Some plagioclase crystals show complex and discontinuous compositional variation, where the low-Ca plagioclase core (An_{36}) is surrounded by relative high-Ca mantle (An_{38-41}) and the outermost rim of the plagioclase is Na-rich with An_{25-27} (Fig. 4d).

5 Geochronology and whole-rock geochemistry

5.1 Zircon U-Pb geochronology

LA-ICP-MS zircon U-Pb data are given in Appendix 3 and presented in Fig. 8.

Zircons in sample XKL12-21 (dioritic dikes) are mostly subhedral and elongated crystals with clear oscillatory zoning (Fig. 8a) with varying Th (281 - 1111 ppm) and U (482 - 1859 ppm) and high Th/U ratios (0.51 - 0.84), suggesting a magmatic origin. Fourteen analyses yield a weighted mean $^{206}Pb/^{238}U$ age of 100.2 ± 1.0 Ma (MSWD = 0.5) (Fig. 8a).

Zircons in sample XKL12-31 (granodiorite) show relatively low and variable Th/U ratios (0.09 - 0.39) because of variably higher U (422 - 2640 ppm) than Th (148 - 584 ppm). Fourteen analyses of zircons give a weighted mean $^{206}Pb/^{238}U$ age of 104.0 ± 1.6 Ma (MSWD = 4.9) (Fig. 8b). The similar age between the dioritic dike and the granodiorite samples imply their genetic link to a common thermal event.

5.2 Whole-rock major and trace elements

Whole-rock major and trace element data of 9 samples (5 dioritic dike and 4 granodiorite samples) are given in Appendix 4.

The dioritic dikes are characterized by varying SiO_2 (55.8 - 66.8 wt%), MgO (1.56 - 6.71 wt%; $Mg^{\#}$ = 0.43 - 0.65), and relatively high alkalis ($K_2O + Na_2O$ = 4.8 - 6.5 wt%), plotting in the gabbroic diorite (XKL12-21), diorite (XKL12-25) and granodiorite (XKL12-26, 27) fields in the TAS diagram (Fig. 9a), respectively. In addition, they show calc-alkaline to high-K calc-alkaline (Fig. 9b) and metaluminous (A/CNK = 0.76 - 1.05) features (Fig. 9c) as well as relative high K_2O/Na_2O (0.55 - 0.84) values (Fig. 9d). In SiO_2 variation diagrams (Fig. 10), most oxides exhibit well defined trends.

Trace elements of the dioritic dikes show enrichment of LILEs (Rb, K, Ba, Pb) and relative depletion of HFSEs (Nb, Ta, Ti, P) (Fig. 11a) with uniform Nb/Ta ratios

(14.9 - 15.0). Chondrite-normalized REE patterns of these samples show varying enrichment of LREEs ($[La/Yb]_N$ = 10.1 - 23.7) and variably fractionated HREEs ($[Dy/Yb]_N$ = 1.25 - 1.66) (Fig. 11b). The samples also display variable Sr anomalies (Sr/Sr* = 0.67 - 1.02) and negative Eu anomalies (Eu/Eu* = 0.74 - 0.85).

The granodiorite samples have relatively high SiO_2 (65.1 - 70.3 wt%) and K_2O + Na_2O (6.4 - 7.3 wt%), plotting in the granodiorite field in the TAS diagram (Fig. 9a) and displaying high-K calc-alkaline characteristics in the K_2O - SiO_2 diagram (Fig. 9b). They have relatively higher A/CNK (1.01 - 1.11) values (Fig. 9c) with metaluminous to peraluminous characteristics and K_2O/Na_2O (1.14 - 1.56) values than those of the dioritic dikes (Fig. 9d). Most major elements also show linear trends with SiO_2 (Fig. 10).

In the primitive mantle normalized trace element diagram, the granodiorite samples also show enrichment of LILEs (Rb, Ba, K, Pb) and depletion of HFSEs (Nb, Ta, Ti, P) (Fig. 11c). Most of these samples show elevated LREEs/HREEs ratios ($[La/Yb]_N$ = 12.4 - 26.8) with significant negative Sr and Eu anomalies (Sr/Sr* = 0.48 - 0.70, Eu/Eu* = 0.57 - 0.69) (Fig. 11c, d). We note that sample XKL12-19 has obvious Zr-Hf depletion (Zr: 25 ppm; Hf: 0.8 ppm) than other samples (Zr: 109 - 287 ppm; Hf: 2.9 - 6.6 ppm) (Fig. 11c; Fig. 12a). Zircon crystallization could explain the Zr-Hf depletion as evidenced by the decreasing Zr/Sm with increasing SiO_2 (excluding this sample; Fig. 12c). However, sample XKL12-32 has the same silica content (68.3 wt%) but higher Zr-Hf concentrations (Zr: 169 ppm; Hf: 4.1 ppm) than sample XKL12-19 (Appendix 4). Meanwhile, sample XKL12-19 shows relatively lower HREEs ($[Dy/Yb]_N$ = 1.72) than other samples ($[Dy/Yb]_N$ = 1.34 - 1.64). Nevertheless, we consider that the Zr-Hf depletion may be due to incomplete digestion of zircons in this sample (Fig. 12b, d).

5.3 Sr-Nd-Hf isotopes

The whole-rock Sr-Nd-Hf isotope data of 6 samples (3 dioritic dike and 3 granodiorite samples) are given in Appendix 5.

The dioritic dikes show relatively uniform initial $^{87}Sr/^{86}Sr$ (0.7066 to 0.7071, calculated at 100 Ma), low $\varepsilon_{Nd}(t)$ (-5.3 to -7.4) and $\varepsilon_{Hf}(t)$ (-3.6 to -6.2). The granodiorite samples show higher initial $^{87}Sr/^{86}Sr$ (0.7087 - 0.7125) (calculated at 104 Ma), and more enriched $\varepsilon_{Nd}(t)$ (-9.5 to -11.6) and $\varepsilon_{Hf}(t)$ (-10.3 to -14.1) than those of dioritic dikes (Fig. 15a). The apparent isotopic differences between the dioritic dike and granodiorite samples indicate their different source origin.

6 Discussion

6.1 Petrogenesis of dioritic dikes

Sample XKL12-21 has the lowest SiO_2 (55.8 wt%), and the highest MgO (6.71 wt%), Ni (52 ppm), Cr (318 ppm) and $Mg^{\#}$ (0.65) among the dioritic dike samples of this study, similar to those high-Mg andesite/diorite (HMD), which is consistent with a mantle source with significant fractional crystallization.

Several petrogenic models exist for HMD, including (1) partial melts from delaminated mafic crust with reaction with mantle peridotite (Chen et al., 2013; Huang et al., 2008; Xu et al., 2002; Xu et al., 2008); (2) direct partial melting of the mantle wedge metasomatized by slab-derived melts/fluids or subducted sediment-derived melts in subduction zones (Castillo, 2008, 2012; Tatsumi, 1989; Yin et al., 2010; Yogodzinski et al., 1995; Zhang et al., 2014); (3) magma mixing or AFC (assimilation and fractional crystallization) processes (Chen et al., 2013; Ma et al., 2012; Moyen et al., 2001; Zhang et al., 2014).

Partial melts from delaminated mafic lower crust with reaction with mantle peridotite usually generate high-Mg diorite with adakitic characteristics (e.g., high Sr > 400 ppm, low Y < 20 ppm, Yb < 2 ppm;) in an intra-continental setting (Castillo, 2012; Defant and Drummond, 1990), while sample XKL12-21 has moderate Sr (520 ppm), high Y (23 ppm) and Yb (2.2 ppm) with no adakitic signatures. Thus, they were unlikely to originate from delaminated lower crust source.

Sample XKL12-21 and other dioritic dike samples show enriched isotope compositions ($^{87}Sr/^{86}Sr_i$: 0.7066 to 0.7071; $\varepsilon_{Nd}(t)$: -5.3 to -7.4; and $\varepsilon_{Hf}(t)$: -3.6 to -6.2) as well as the positive and negative correlations between SiO_2 and $^{87}Sr/^{86}Sr_i$ and $\varepsilon_{Nd}(t)$ respectively (Fig. 14a, b). If these dioritic dikes were derived from partial melting of a depleted asthenospheric mantle source, then significant continental crustal contamination would be needed as shown by a simple two-component mixing model requiring incorporation of ~40% to 45% crustal components (Fig. 15a). However, such a voluminous contamination would modify major element compositions of these rocks. Indeed, the content of SiO_2 of these dioritic dike samples exhibit a relative large compositional variation from 55.8 wt% to 66.8 wt%, which is inconsistent with such a voluminous mixing/assimilation. Besides, the dioritic dikes have more enriched incompatible element abundances than those of the bulk continental crust (BCC) (Fig. 11a, b; Rudnick and Gao, 2003), suggesting that the mantle source must have experienced a metasomatic process. Therefore, an enriched mantle source would be required.

According to the enriched incompatible element abundances and isotopes of the dioritic dikes, it is possible that they could be derived from metasomatized sub-continental lithospheric mantle, but such melts would be produced at post-collisional stages and generate potassic or ultralpotassic rocks with extremely

high alkali contents than these dike rocks (Guo et al., 2006; Huang et al., 2010; Jiang et al., 2006; Liu et al., 2014, 2015). Additionally, another main magmatism peak during the Miocene has also been identified for the Karakoram batholith represented by the Karibasheng and Kuzigan plutons (Fig. 1a, in the northern Hongqilafu pluton) with alkali-rich characteristics, which may indeed have derived from partial melting of the veined metasomatized lithospheric mantle in a post-collisional environment (Jiang et al., 2012). Therefore, the dioritic dikes in the Hongqilafu pluton are considered unlikely to have generated by partial melting of metasomatized sub-continental lithospheric mantle. A subduction setting (see below) is more likely.

We suggest that this enriched mantle end-member could be mantle wedge metasomatized by slab-derived melts/fluids or subducted sediment-derived melts. The $^{87}Sr/^{86}Sr_i$ show obvious linear relation with 1/Sr (Fig. 15b), indicating the possibility of magma mixing or AFC processes (DePaolo, 1981). But simple mixing line between metasomatized mantle wedge (EM) and lower continental crust (LCC) is far away from the actual linear trend of the dioritic dikes (Fig. 15b).

With the mineralogy and geochemistry all considered, we infer that that the primitive magma parental to the dioritic dikes is more likely to have experienced variable degree of AFC processes as supported by several lines of evidence:

(i) The rock types and compositions of these dioritic dikes range from gabbroic diorite, diorite porphyry to granodiorite porphyry, exhibiting a continuous compositional trends from intermediate to felsic rocks, suggesting the effect of fractional crystallization as evidenced by modal mineralogy and elemental systematics (Fig. 3; Fig. 10). The decreasing Sr with increasing SiO_2 and the decreasing Eu/Eu* with decreasing Sr, are consistent with plagioclase crystallization (Fig. 13a, b).

(ii) Mineralogically, the dioritic dikes show compositional and textural disequilibrium,

marked by large compositional variation of plagioclase (Fig. 7) and coexisting high-Ca and low-Ca plagioclase in single thin sections (Fig. 3c, d; Fig. S1a-e). The clinopyroxene crystals also exhibit large compositional variation (Fig. 3a, b; Fig. 6). The amphiboles have multiple and reverse zoning (Fig. 3e, f), suggesting that the mafic magma parental to the dioritic dikes have experienced open system processes with assimilation of continental crustal material and replenishment of new, more primitive mafic magma during magma evolution.

(iii) The granodiorite samples are probably different products of the same thermal event induced by dioritc dikes-forming magmas (see below). When primitive magma parental to the dioritic dikes underplated the lower continental crust, assimilation with the crustal material becomes inevitable, which is apparent as shown in SiO_2 vs. $^{87}Sr/^{86}Sr_i$ and $\varepsilon_{Nd}(t)$ diagrams respectively (Fig. 14a, b).

As discussed above, the dioritic dikes in the Hongqilafu pluton were most likely generated by partial melting of mantle wedge metasomatized by subducted/subducting slab or sediment-derived components, followed by AFC processes with clinopyroxene, amphibole and plagioclase fractional crystallization as well as assimilation of lower continental crust, which are in accord with our AFC modeling (Fig. 15b).

6.2 Petrogenesis of granodiorite

The granodiorite samples have more enriched isotope compositions ($^{87}Sr/^{86}Sr_i$: 0.7087 to 0.7125; $\varepsilon_{Nd}(t)$: -9.5 to -11.6; and $\varepsilon_{Hf}(t)$: -10.3 to -14.1) than dioritic dikes, ruling out their origin from fractional crystallization from the magma parental to the dioritic dikes. They were more likely to have derived from a crustal source than a mantle source.

The main source for magma parental to the granodiorite is predicted to be lower

continental crust. Generally, partial melting of upper crustal material (pelitic rocks) would generate peraluminous (A/CNK > 1.1) S-type granites containing Al-rich minerals such as garnet or cordierite (Sylvester, 1998), yet these Al-rich minerals are absent and the granodiorite samples have relatively low A/CNK values (1.01 - 1.11). The relatively low Sr (272 - 454 ppm) and Sr/Y (13.1 - 23.4) and the relatively flat REE patterns of the granodiorite preclude the petrogenesis of adakite or adakitic rocks, i.e., they were unlikely to derive from thickened lower crust or delaminated lower crust with garnet as residual phase (Chung et al., 2003; Wang et al., 2005, 2007). Therefore, the source region of the granodiorite is relatively shallow (< 40 km) without having garnet as a residual or liquidus phase. The tectonic-thermal setting for the generation of dioritic dikes and granodiorite could be in an active continental margin subduction setting.

As discussed above, the dioritic dikes originated from partial melting of a metasomatized mantle wedge source, and the ascent of mafic magma parental to the dioritic dikes would underplate the lower continental crust and induce its partial melting, forming felsic magma parental to the granodiorite.

In Fig. 14, the granodiorite samples show increasing $^{87}Sr/^{86}Sr_i$ and decreasing $\varepsilon_{Nd}(t)$ with increasing SiO_2, and the slope of $^{87}Sr/^{86}Sr$ vs. SiO_2 or $\varepsilon_{Nd}(t)$ vs. SiO_2 of the granodiorite samples are steeper than those of dioritic dikes. It could be mistakenly interpreted that the felsic magma parental to the granodiorite experienced varying extent of upper continental crustal assimilation during ascent. We consider this scenario to be unlikely because such apparent crustal contamination is difficult for granitic melts without sufficient heat energy, and the extent of crustal contamination is limited. Thus, the linear trends between SiO_2 and Sr-Nd isotopes (Fig. 14a, b) are more likely caused by the mixing process between mantle-derived mafic melt and

lower continental crust-derived felsic melt.

Contributions from magma parental to the dioritic dikes (i.e., mantle-derived melt) are evidenced by (i) the disequilibrium features reflected by the discontinuous compositional variation in the plagioclase crystals of the granodiorite (Fig. 4; Fig. 5b; Fig. S2); (ii) the granodiorite samples show relative higher $Mg^{\#}$ (0.41 - 0.50) than experimental pure crustal melt (Rapp and Watson, 1995); (iii) the granodiorite samples have relatively variable Cr (11 - 50 ppm) and Ni (2 - 21 ppm) concentrations; (iv) the linear $^{87}Sr/^{86}Sr_i$ vs. 1/Sr relationship of the granodiorite samples (Fig. 15c), which implies the mixing between mantle-derived melt and crustal melt.

In addition, fractional crystallization plays a dominant role in the magma evolution. Plagioclase fractionation is also evidenced by the decreasing Sr with increasing SiO_2 and the decreasing Eu/Eu* with decreasing Sr (Fig. 13a, b). Fractional crystallization of zircon is also obvious and important in felsic magma evolution evidenced by rapid decreasing of Zr/Sm with increasing SiO_2 and with decreasing HREEs respectively, because zircons have strong preference for HREEs (Fig. 12).

In summary, the underplated mantle-derived magma parental to the dioritic dikes induced the lower continental crust to melt (providing heat and material), generating the granodiorite in the Hongqilafu pluton.

It should be noted that the dioritic dikes intruding the felsic pluton are significantly (~4 Myrs) younger. Thus, the thermal event would last for several million years. And the mantle-derived magma periodically underplated the lower continental crust to generate the observed granodiorite, while a more recent pulse of mantle-derived melt (with AFC histories) generated the dioritic dikes and intruded the granodiorite.

6.3 Implication for crust-mantle interaction in northwestern Tibetan Plateau

According to previous studies, the Kohistan-Ladakh intra-oceanic island arc (KLA) was formed from the northward subduction of Neo-Tethyan oceanic crust lasting from the late Mesozoic until to the final India-Eurasia collision at ~50 Ma (Bouilhol et al., 2013; Burg, 2011). A second subduction zone existed to the north of the KLA that the Shyok back-arc oceanic crust subducted beneath the KT and induced immense continental-arc magmatism represented by the voluminous Early Cretaceous Karakoram batholith (Bouilhol et al., 2013; Ravikant et al., 2009). During this period, large quantities of tonalite and granodiorite magmas of ~120 Ma to ~100 Ma were generated, probably derived from the Karakoram basement with input of mantle-derived melt (Ravikant, 2006; Ravikant et al., 2009). The ~104 Ma granodiorite in the Hongqilafu pluton in this study also support the existence of this stage of granitic magmatism related to the subduction of the Shyok back-arc oceanic crust beneath the KT. As mentioned above, another main intrusive stage for the Karakoram batholith occurred during the Miocene which mainly consists of leucogranites and some K-rich granites (Ravikant et al., 2009; Jiang et al., 2012). The rarity of Late Cretaceous and Early Cenozoic granitoids within the Karakoram batholith may be linked with the closure of Shyok back-arc basin.

However, the clear evidence of ophiolite in the Shyok Suture Zone (SSZ) is lacking and parts of the SSZ were reactivated by tectonic event during the Early Miocene (Brookfield and Reynolds, 1990; Weinberg and Dunlap, 2000), so the timing of Shyok basin closure is still ambiguous and debatable. Estimates of the SSZ closure timing range from ~110 Ma (Jiang et al., 2014), ~83 - 93 Ma (Clift et al., 2002; Ravikant et al., 2009), and even later at ~40 Ma (Bouilhol et al., 2013) based on the geochronology and geochemistry of related plutonic rocks. Ravikant et al. (2009) also

proposed that the KLA became an active continental margin of the Karakoram terrane since the closure of the Shyok back-arc basin around Middle Cretaceous. When the Shyok back-arc basin closed, the magmatism related to the subduction of the Shyok back-arc oceanic crust had been temporarily terminated.

In this study, having precluded the sub-continental lithospheric mantle source for the dioritic dikes and the petrogenesis of adakite/adakitic rocks for the granodiorite in the Hongqilafu pluton, we infer that the generation of the Hongqilafu pluton represents a large thermal event of mantle melting with induced crust melting and granitic magmatism lasting for several million years at an active continental margin subduction setting. This also indicates the timing of Shyok basin closure occurred after ~100 Ma at least. The collision between the KLA and the KT must be significantly later than previously thought, which further constraints are needed based on other geological evidences.

7 Conclusions

(1) The granodiorite and associated dioritic dikes in the Hongqilafu pluton are dated at ~104 Ma and ~100 Ma, respectively.

(2) The dioritic dikes range from gabbroic diorite, diorite porphyry to granodiorite porphyry, exhibiting a compositional spectrum from intermediate to the more felsic compositions, while their mineral chemistries reflect some disequilibrium features. They are characterized by enriched incompatible elements and Sr-Nd-Hf isotopes. They were generated by partial melting of mantle wedge metasomatized by the subducted/subducting slab or sediment-derived components, followed by AFC processes with clinopyroxene, amphibole and plagioclase fractional crystallization as well as assimilation of lower continental crust.

(3) The mantle-wedge derived magma parental to the dioritic dikes underplated and induced the lower continental crust to melt, forming the felsic crustal magma parental to the granodiorite with mantle melt signatures.

(4) The generation of the Hongqilafu pluton represents a large thermal event of mantle melting with induced crust melting lasting for several million years at an active continental margin subduction setting. This indicates the timing of Shyok basin closure occurred after ~100 Ma at least. The collision between the KLA and the KT must be significantly later than previously thought.

Acknowledgments

This work was supported by the National Natural Science Foundation of China (NSFC Grants 41130314, 91014003), Chinese Academy of Sciences (Innovation Grant Y42217101L) and grants from regional and local authorities (Shandong Province and City of Qingdao). We thank Xiaolong Huang, Yang Yu, Pengli He, Jinju Liu for their field assistance. Lei Ye and Guorui Zhang are thanked for their help with sample preparation. We acknowledge Li Su for the assistance with whole rock major and trace elements analysis, Yongsheng Liu and Zhaochu Hu for assistance with zircon analysis, and Jinlong Ma with isotopes analysis. We also thank Mingwu Liu with electron microprobe analysis.

References

Allègre, C.J., Rousseau, D., 1984. The growth of the continent through geological time studied by Nd isotope analysis of shales. Earth and Planetary Science Letters 67, 19-34.

Armstrong, R.L., Harmon, R.S., 1981. Radiogenic isotopes: the case for crustal

recycling on a near-steady-state no-continental-growth Earth and discussion. Philosophical Transactions of the Royal Society of London A: Mathematical, Physical and Engineering Sciences 301, 443-472.

Bergantz, G.W., 1989. Underplating and partial melting: implications for melt generation and extraction. Science 245, 1093-1095.

Bhutani, R., Pande, K., Desai, N., 2003. Age of the Karakoram fault activation: ^{40}Ar-^{39}Ar geochronological study of Shyok suture zone in northern Ladakh, India. Current Scinece 84, 1454-1458.

Bouilhol, P., Jagoutz, O., Hanchar, J.M., Dudas, F.O., 2013. Dating the India-Eurasia collision through arc magmatic records. Earth and Planetary Science Letters 366, 163-175.

Brookfield, M.E., Reynolds, P.H., 1990. Miocene ^{40}Ar/^{39}Ar ages from the Karakorum Batholith and Shyok Mélange, northern Pakistan, indicate late Tertiary uplift and southward displacement. Tectonophysics 172, 155-167.

Burg, J.P., 2011. The Asia-Kohistan-India collision: review and discussion, Arc-Continent Collision. Springer, pp. 279-309.

Cao, K., Wang, G.C., Bernet, M., van der Beek, P., Zhang, K.X., 2015. Exhumation history of the West Kunlun Mountains, northwestern Tibet: Evidence for a long-lived, rejuvenated orogen. Earth and Planetary Science Letters 432, 391-403.

Castillo, P.R., 2008. Origin of the adakite-high-Nb basalt association and its implications for postsubduction magmatism in Baja California, Mexico. Geological Society of America Bulletin 120, 451-462.

Castillo, P.R., 2012. Adakite petrogenesis. Lithos 134, 304-316.

Chen, B., Chen, Z.C., Jahn, B.M., 2009. Origin of mafic enclaves from the Taihang

Mesozoic orogen, north China craton. Lithos 110, 343-358.

Chen, B., Jahn, B.M., Suzuki, K., 2013. Petrological and Nd-Sr-Os isotopic constraints on the origin of high-Mg adakitic rocks from the North China Craton: Tectonic implications. Geology 41, 91-94.

Chung, S.L., Liu, D.Y., Ji, J.Q., Chu, M.F., Lee, H.Y., Wen, D.J., Lo, C.H., Lee, T.Y., Qian, Q., Zhang, Q., 2003. Adakites from continental collision zones: melting of thickened lower crust beneath southern Tibet. Geology 31, 1021-1024.

Clift, P.D., Hannigan, R., Blusztajn, J., Draut, A.E., 2002. Geochemical evolution of the Dras-Kohistan Arc during collision with Eurasia: evidence from the Ladakh Himalaya, India. Island Arc 11, 255-273.

Clift, P.D., Vannucchi, P., Morgan, J.P., 2009. Crustal redistribution, crust-mantle recycling and Phanerozoic evolution of the continental crust. Earth-Science Reviews 97, 80-104.

Collerson, K.D., Kamber, B.S., 1999. Evolution of the continents and the atmosphere inferred from Th-U-Nb systematics of the depleted mantle. Science 283, 1519-1522.

Conrad, C.P., Molnar, P., 1997. The growth of Rayleigh-Taylor-type instabilities in the lithosphere for various rheological and density structures. Geophysical Journal International 129, 95-112.

Coward, M.P., Butler, R.W.H., Khan, M.A., Knipe, R.J., 1987. The tectonic history of Kohistan and its implications for Himalayan structure. Journal of the Geological Society 144, 377-391.

Defant, M.J., Drummond, M.S., 1990. Derivation of some modern arc magmas by melting of young subducted lithosphere. Nature 347, 662-665.

DePaolo, D.J., 1981. Trace element and isotopic effects of combined wallrock

assimilation and fractional crystallization. Earth and Planetary Science Letters 53, 189-202.

Fraser, J.E., Searle, M.P., Parrish, R.R., Noble, S.R., 2001. Chronology of deformation, metamorphism, and magmatism in the southern Karakoram Mountains. Geological Society of America Bulletin 113, 1443-1455.

Gaetani, M., 1997. The Karakorum block in central Asia, from Ordovician to Cretaceous. Sedimentary Geology 109, 339-359.

Guo, Z.F., Wilson, M., Liu, J.Q., Mao, Q., 2006. Post-collisional, potassic and ultrapotassic magmatism of the northern Tibetan Plateau: Constraints on characteristics of the mantle source, geodynamic setting and uplift mechanisms. Journal of Petrology 47, 1177-1220.

Heuberger, S., Schaltegger, U., Burg, J.P., Villa, I.M., Frank, M., Dawood, H., Hussain, S., Zanchi, A., 2007. Age and isotopic constraints on magmatism along the Karakoram-Kohistan Suture Zone, NW Pakistan: Evidence for subduction and continued convergence after India-Asia collision. Swiss Journal of Geosciences 100, 85-107.

Hofmann, A.W., 1988. Chemical differentiation of the Earth: the relationship between mantle, continental crust, and oceanic crust. Earth and Planetary Science Letters 90, 297-314.

Hu, P.Y., Zhai, Q.G., Jahn, B.M., Wang, J., Li, C., Lee, H.Y., Tang, S.H., 2015. Early Ordovician granites from the South Qiangtang terrane, northern Tibet: Implications for the early Paleozoic tectonic evolution along the Gondwanan proto-Tethyan margin. Lithos 220, 318-338.

Huang, F., Li, S.G., Dong, F., He, Y.S., Chen, F.K., 2008. High-Mg adakitic rocks in the Dabie orogen, central China: implications for foundering mechanism of

lower continental crust. Chemical Geology 255, 1-13.

Huang, X.L., Niu, Y.L., Xu, Y.G., Chen, L.L., Yang, Q.J., 2010. Mineralogical and geochemical constraints on the petrogenesis of post-collisional potassic and ultrapotassic rocks from western Yunnan, SW China. Journal of Petrology 51, 1617-1654.

Jiang, Y.H., Jiang, S.Y., Ling, H.F., Dai, B.Z., 2006. Low-degree melting of a metasomatized lithospheric mantle for the origin of Cenozoic Yulong monzogranite-porphyry, east Tibet: Geochemical and Sr-Nd-Pb-Hf isotopic constraints. Earth and Planetary Science Letters 241, 617-633.

Jiang, Y.H., Liao, S.Y., Yang, W.Z., Shen, W.Z., 2008. An island arc origin of plagiogranites at Oytag, western Kunlun orogen, northwest China: SHRIMP zircon U-Pb chronology, elemental and Sr-Nd-Hf isotopic geochemistry and Paleozoic tectonic implications. Lithos 106, 323-335.

Jiang, Y.H., Liu, Z., Jia, R.Y., Liao, S.Y., Zhou, Q., Zhao, P., 2012. Miocene potassic granite-syenite association in western Tibetan Plateau: Implications for shoshonitic and high Ba-Sr granite genesis. Lithos 134-135, 146-162.

Jiang, Y.H., Liu, Z., Jia, R.Y., Liao, S.Y., Zhao, P., Zhou, Q., 2014. Origin of Early Cretaceous high-K calc-alkaline granitoids, western Tibet: implications for the evolution of the Tethys in NW China. International Geology Review 56, 88-103.

Kay, R.W., Kay, S.M., 1993. Delamination and delamination magmatism. Tectonophysics 219, 177-189.

Leake, B.E., Wooley, A.R., Arps, C.E.S., Birch, W.D., Gilbert, M.C., Grice, J.D., Hawthorne, F.C., Kato, A., et al., 1997. Nomenclature of amphiboles: report of the Subcommittee on Amphiboles of the International Mineralogical Association, commission on new minerals and mineral names. The Canadian Mineralogist 35,

219-246.

Lee, C.T.A., Anderson, D.L., 2015. Continental crust formation at arcs, the arclogite "delamination" cycle, and one origin for fertile melting anomalies in the mantle. Science Bulletin 60, 1141-1156.

Lee, C.T.A., 2012. Physics and chemistry of deep continental crust recycling. The Crust 4.

Li, X.H., Li, Z.X., Wingate, M.T.D., Chung, S.L., Liu, Y., Lin, G.C., Li, W.X., 2006. Geochemistry of the 755Ma Mundine Well dyke swarm, northwestern Australia: part of a Neoproterozoic mantle superplume beneath Rodinia? Precambrian Research 146, 1-15.

Lin, W.W., Peng, L.J., 1994. The estimation of Fe^{3+} and Fe^{2+} contents in amphibole and biotite from EMPA data. Journal of Changchun University Earth Sciences 24, 155-162 (in Chinese with English abstract).

Liu, D., Zhao, Z.D., Zhu, D.C., Niu, Y.L., DePaolo, D.J., Harrison, T.M., Mo, X.X., Dong, G.C., Zhou, S., Sun, C.G., Zhang, Z.C., Liu, J.L., 2014. Postcollisional potassic and ultrapotassic rocks in southern Tibet: Mantle and crustal origins in response to India-Asia collision and convergence. Geochimica et Cosmochimica Acta 143, 207-231.

Liu, D., Zhao, Z.D., Zhu, D.C., Niu, Y.L., Widom, E., Teng, F.Z., DePaolo, D.J., Ke, S., Xu, J.F., Wang, Q., Mo, X.X., 2015. Identifying mantle carbonatite metasomatism through Os-Sr-Mg isotopes in Tibetan ultrapotassic rocks. Earth and Planetary Science Letters 430, 458-469.

Liu, Y.S., Gao, S., Hu, Z.C., Gao, C.C., Zong, K.Q., Wang, D.B., 2010a. Continental and oceanic crust recycling-induced melt-peridotite interactions in the Trans-North China Orogen: U-Pb dating, Hf isotopes and trace elements in

zircons from mantle xenoliths. Journal of Petrology 51, 537-571.

Liu, Y.S., Hu, Z.C., Zong, K.Q., Gao, C.G., Gao, S., Xu, J., Chen, H.H., 2010b. Reappraisement and refinement of zircon U-Pb isotope and trace element analyses by LA-ICP-MS. Chinese Science Bulletin 55, 1535-1546.

Ludwig, K., 2012. User's manual for Isoplot version 3.75-4.15: a geochronological toolkit for Microsoft. Excel Berkley Geochronological Center Special Publication.

Ma, C., Xiao, W.J., Windley, B.F., Zhao, G.P., Han, C.M., Zhang, J.E., Luo, J., Li, C., 2012. Tracing a subducted ridge-transform system in a late Carboniferous accretionary prism of the southern Altaids: Orthogonal sanukitoid dyke swarms in Western Junggar, NW China. Lithos 140, 152-165.

Ma, J.L., Wei, G.J., Liu, Y., Ren, Z.Y., Xu, Y.G., Yang, Y.H., 2013a. Precise measurement of stable ($\delta^{88/86}$Sr) and radiogenic (^{87}Sr/^{86}Sr) strontium isotope ratios in geological standard reference materials using MC-ICP-MS. Chinese Science Bulletin 58, 3111-3118.

Ma, J.L., Wei, G.J., Liu, Y., Ren, Z.Y., Xu, Y.G., Yang, Y.H., 2013b. Precise measurement of stable neodymium isotopes of geological materials by using MC-ICP-MS. Journal of Analytical Atomic Spectrometry 28, 1926-1931.

Middlemost, E.A., 1994. Naming materials in the magma/igneous rock system. Earth-Science Reviews 37, 215-224.

Mo, X.X., Hou, Z.,Q. Niu, Y.L., Dong, G.C., Qu, X.M., Zhao, Z.D., Yang, Z.M., 2007. Mantle contributions to crustal thickening during continetal collision: evidence from Cenozoic igneous rocks in southern Tibet. Lithos 96, 225-242.

Mo, X.X., Niu, Y.L., Dong, G.C., Zhao, Z.D., Hou, Z.Q., Zhou, S., Ke, S., 2008. Contribution of syncollisional felsic magmatism to continental crust growth: A

case study of the Paleogene Linzizong volcanic Succession in southern Tibet. Chemical Geology 250, 49-67.

Morimoto, N., Fabries, J., Ferguson, A.K., Ginzburg, I.V., Ross, M., Seifert, F.A., Zussman, J., Aoki, K., Gottardi, G., 1988. Nomenclature of pyroxenes. American Mineralogist 73, 1123-1133.

Moyen, J.F., Martin, H., Jayananda, M., 2001. Multi-element geochemical modelling of crust-mantle interactions during late-Archaean crustal growth: the Closepet granite (South India). Precambrian Research 112, 87-105.

Niu, Y.L., Zhao, Z.D., Zhu, D.C., Mo, X.X., 2013. Continental collision zones are primary sites for net continental crust growth - A testable hypothesis. Earth-Science Reviews 127, 96-110.

Pan, G.T., Ding, J., Yao, D.S., Wang, L.Q., 2004. Guidebook of 1:1,500,000 geological map of the Qinghai-Xizang (Tibet) Plateau and adjacent areas. Cartographic Publishing House, Chengdu, China, pp. 1-148.

Peccerillo, A., Taylor, S.R., 1976. Geochemistry of Eocene calc-alkaline volcanic rocks from the Kastamonu area, northern Turkey. Contributions to Mineralogy and Petrology 58, 63-81.

Rapp, R.P., Watson, E.B., 1995. Dehydration melting of metabasalt at 8-32 kbar: implications for continental growth and crust-mantle recycling. Journal of Petrology 36, 891-931.

Ravikant, V., 2006. Utility of Rb-Sr geochronology in constraining Miocene and Cretaceous events in the eastern Karakoram, Ladakh, India. Journal of Asian Earth Sciences 27, 534-543.

Ravikant, V., Wu, F.Y., Ji, W.Q., 2009. Zircon U-Pb and Hf isotopic constraints on petrogenesis of the Cretaceous-Tertiary granites in eastern Karakoram and

Ladakh, India. Lithos 110, 153-166.

Rolland, Y., Pecher, A., Picard, C., 2000. Middle Cretaceous back-arc formation and arc evolution along the Asian margin: the Shyok Suture Zone in northern Ladakh (NW Himalaya). Tectonophysics 325, 145-173.

Rudnick, R.L., Gao, S., 2003. Composition of the continental crust. Treatise on geochemistry 3, 1-64.

Schaltegger, U., Frank, M., Burg, J.P., 2003. A 120 million years record of magmatism and crustal melting in the Kohistan Batholith. Geophysical Research Abstract; EGS-AGU-EUG Joint Assembly 5:EAE03-A-08307.

Searle, M.P., Parrish, R.R., Thow, A.V., Noble, S.R., Phillips, R.J., Waters, D.J., 2010. Anatomy, age and evolution of a collisional mountain belt: the Baltoro granite batholith and Karakoram Metamorphic Complex, Pakistani Karakoram. Journal of the Geological Society 167, 183-202.

Song, S.G., Su, L., Li, X.H., Zhang, G.B., Niu, Y.L., Zhang, L.F., 2010. Tracing the 850-Ma continental flood basalts from a piece of subducted continental crust in the North Qaidam UHPM belt, NW China. Precambrian Research 183, 805-816.

Sun, S.S., McDonough, W.F., 1989. Chemical and isotopic systematics of oceanic basalts: implications for mantle composition and processes. Geological Society, London, Special Publications 42, 313-345.

Sylvester, P.J., 1998. Post-collisional strongly peraluminous granites. Lithos 45, 29-44.

Tatsumi, Y., 1989. Boninites and high-Mg andesites: tectonics and petrogenesis. Boninites and related rocks, 50-71.

Taylor, S.R., McLennan, S.M., 1995. The geochemical evolution of the continental crust. Reviews of Geophysics 33, 241-265.

Thakur, V.C., Misra, D.K., 1984. Tectonic framework of the Indus and Shyok suture zones in eastern Ladakh, northwest Himalaya. Tectonophysics 101, 207-220.

Wang, Q., McDermott, F., Xu, J.F., Bellon, H., Zhu, Y.T., 2005. Cenozoic K-rich adakitic volcanic rocks in the Hohxil area, northern Tibet: lower-crustal melting in an intracontinental setting. Geology 33, 465-468.

Wang, Q., Wyman, D.A., Xu, J.F., Jian, P., Zhao, Z.H., Li, C.F., Xu, W., Ma, J.L., He, B., 2007. Early Cretaceous adakitic granites in the Northern Dabie Complex, central China: implications for partial melting and delamination of thickened lower crust. Geochimica et Cosmochimica Acta 71, 2609-2636.

Wang, Z.H., Sun, S., Li, J.L, Hou, Q.L, 2002. Petrogenesis of tholeiite associations in Kudi ophiolite (western Kunlun Mountains, northwestern China): implications for the evolution of back-arc basins. Contributions to Mineralogy and Petrology 143, 471-483.

Weinberg, R.F., Dunlap, W.J., 2000. Growth and deformation of the Ladakh Batholith, northwest Himalayas: implications for timing of continental collision and origin of calc-alkaline batholiths. The Journal of Geology 108, 303-320.

Wu, F.Y., Ji, W.Q., Sun, D.H., Yang, Y.H., Li, X.H., 2012. Zircon U-Pb geochronology and Hf isotopic compositions of the Mesozoic granites in southern Anhui Province, China. Lithos 150, 6-25.

Xia, Y., Xu, X.S., Zou, H.B., Liu, L., 2014. Early Paleozoic crust–mantle interaction and lithosphere delamination in South China Block: Evidence from geochronology, geochemistry, and Sr-Nd-Hf isotopes of granites. Lithos 184, 416-435.

Xiao, W.J., Windley, B.F., Liu, D.Y., Jian, P., Liu, C.Z., Yuan, C., Sun, M., 2005. Accretionary tectonics of the Western Kunlun Orogen, China: a Paleozoic-early

Mesozoic, long-lived active continental margin with implications for the growth of southern Eurasia. The Journal of Geology 113, 687-705.

Xu, J.F., Shinjo, R., Defant, M.J., Wang, Q., Rapp, R.P., 2002. Origin of Mesozoic adakitic intrusive rocks in the Ningzhen area of east China: partial melting of delaminated lower continental crust? Geology 30, 1111-1114.

Xu, W.L., Hergt, J.M., Gao, S., Pei, F.P., Wang, W., Yang, D.B., 2008. Interaction of adakitic melt-peridotite: Implications for the high-$Mg^{\#}$ signature of Mesozoic adakitic rocks in the eastern North China Craton. Earth and Planetary Science Letters 265, 123-137.

Yang, J.H., Wu, F.Y., Wilde, S.A., Xie, L.W., Yang, Y.H., Liu, X.M., 2007. Tracing magma mixing in granite genesis: in situ U-Pb dating and Hf-isotope analysis of zircons. Contributions to Mineralogy and Petrology 153, 177-190.

Yin, A., Harrison, T.M., Murphy, M.A., Grove, M., Nie, S., Ryerson, F.J., Wang, X.F., Chen, Z.L., 1999. Tertiary deformation history of southeastern and southwestern Tibet during the Indo-Asian collision. Geological Society of America Bulletin 111, 1644-1664.

Yin, J.Y., Yuan, C., Sun, M., Long, X.P., Zhao, G.C., Wong, K.P., Geng, H.Y., Cai, K.D., 2010. Late Carboniferous high-Mg dioritic dikes in Western Junggar, NW China: geochemical features, petrogenesis and tectonic implications. Gondwana Research 17, 145-152.

Yogodzinski, G.M., Kay, R.W., Volynets, O.N., Koloskov, A.V., Kay, S.M., 1995. Magnesian andesite in the western Aleutian Komandorsky region: implications for slab melting and processes in the mantle wedge. Geological Society of America Bulletin 107, 505-519.

Zanchi, A., Gaetani, M., 2011. The geology of the Karakoram range, Pakistan: the

new 1:100,000 geological map of Central-Western Karakoram. Italian Journal of Geosciences 130, 161-262.

Zhang, J.Y., Ma, C.Q., Xiong, F.H., Liu, B., Li, J.W., Pan, Y.M., 2014. Early Paleozoic high-Mg diorite-granodiorite in the eastern Kunlun Orogen, western China: Response to continental collision and slab break-off. Lithos 210, 129-146.

Zhang, Y., Niu, Y.L., Hu, Y., Liu, J.J., Ye, L., Kong, J.J., Duan, M., 2016. The syncollisional granitoid magmatism and continental crust growth in the West Kunlun Orogen, China - Evidence from geochronology and geochemistry of the Arkarz pluton. Lithos 245, 191-204.

Zhu, D.C., Zhao, Z.D., Niu, Y.L., Dilek, Y., Hou, Z.Q., Mo, X.X., 2013. The origin and pre-Cenozoic evolution of the Tibetan Plateau. Gondwana Research 23, 1429-1454.

Zindler, A., Staudigel, H., Batiza, R., 1984. Isotope and trace element geochemistry of young Pacific seamounts: implications for the scale of upper mantle heterogeneity. Earth and Planetary Science Letters 70, 175-195.

Figure Captions

Fig. 1 (a) Simplified geological map showing the distribution of granitoids with varying ages on the northwestern Tibetan Plateau (modified from Bouilhol et al., 2013, Ravikant et al., 2009 and Zhang et al., 2016). (b) Geological map of the Hongqilafu pluton. Abbreviations are explained as follows, NKT - North Kunlun Terrane; OKS - Oytag-Kudi-Qimanyute Suture; SKT - Sorth Kunlun Terrane; MKS - Mazha-Kangxiwa-Anyemaqen Suture; TST - Tashkurghan-Tianshuihai Terrane (TST); HQS - Hongshanhu-Qiaoertianshan-Jinshajiang Suture; QTT - Qiangtang Terrane;

BNS - Bangonghu-Nujiang Suture; TMF - Tirich Mir Fault; SSZ - Shyok Suture Zone; ITSZ - Indus-Tsangpo Suture Zone. Ages of Karibashen pluton and Kuzigan pluton are from Jiang et al., (2012).

Fig. 2 (a), (b) Field photos showing the dioritic dikes intruding the granodiorite with sharp boundary.

Fig. 3 Photomicrographs of the dioritic dikes with disequilibrium features. (a), (b) clinopyroxene phenocrysts showing large MgO content variation (sample XKL12-21); (c), (d) High-Ca and low-Ca plagioclase phenocrysts coexisting in single thin sections (sample XKL12-21); (e), (f) Multiple and reverse zoned amphibole phenocrysts containing plagioclase and K-feldspar, respectively (sample XKL12-25). Cpx-clinopyroxene; Amp-amphibole; Pl-Plagioclase; Bt-Biotite; Chl-Chlorite. Small circles are spots for mineral compositional analysis with the numbers nearby representing MgO contents (wt%) of clinopyroxene, An contents of plagioclase, Or contents of K-feldspar and $Mg^{\#}$ (= 100*Mg/[Mg+Fe^{2+}]) of amphibole, respectively.

Fig. 4 Photomicrographs of the granodiorite. (a) Felsic mineral assemblage as indicated (sample XKL12-19); (b) K-feldspar with Carlsbad twin (sample XKL12-24); (c) Porphyritic texture with plagioclase, biotite and quartz phenocrysts, and the matrix consisting of fine-grained plagioclase and quartz (sample XKL12-29); (d) Plagioclase zoning with relatively low An contents (sample XKL12-32). Small circles are spots for electron microprobe analysis (EPMA) with An/Or contents as indicated.

Fig. 5 Chemical characteristics of minerals for the dioritic dikes and granodiorite. (a),

(b) Ab-Or-An diagram for feldspar. Ab-albite; Or-potassium feldspar; An-anorthite; Ol-oligoclase; And-andesine; La-labradorite; By-bytownite; (c) $CaSiO_3$-$MgSiO_3$-$FeSiO_3$ diagram showing the compositions of pyroxene (Morimoto et al., 1988); (d) Amphibole classification diagram for the dioritic dike samples (Leake et al., 1997).

Fig. 6 Major element compositions of clinopyroxene of the dioritic dike samples. (a) Cr_2O_3 vs. MgO; (b) TFeO (total Fe) vs. MgO.

Fig. 7 Major element compositions of feldspars from the dioritic dike and granodiorite samples. (a) CaO vs. SiO_2; (b) Al_2O_3 vs. SiO_2; (c) Na_2O vs. SiO_2; (d) An contents in feldspar vs. SiO_2 in whole-rock, showing large compositional variation of feldspars for both the dioritic dike and granodiorite samples.

Fig. 8 LA-ICP-MS zircon U-Pb concordia diagrams for the dioritic dike (a) and granodiorite samples (b).

Fig. 9 (a) The total alkali vs. silica (TAS) diagram (Middlemost, 1994); (b) The K_2O vs. SiO_2 diagram (Peccerillo and Taylor, 1976); (c) The A/NK vs. A/CNK diagram; (d) The Na_2O vs. K_2O diagram (Peccerillo and Taylor, 1976). Red circles are our data in this study for the granodiorite, and the grey circles are the literature data for the granodiorite (Jiang et al., 2014). Blue squares are our data in this study for the dioritic dike samples.

Fig. 10 SiO_2 variation diagrams for major element oxides of both the dioritic dike and

granodiorite samples.

Fig. 11 (a), (c) Primitive mantle normalized (Sun and McDonough, 1989) trace-element patterns for the dioritic dike and granodiorite samples, respectively. (b), (d) Chondrite-normalized (Sun and McDonough, 1989) rare earth element (REE) patterns for both the dioritic dike and granodiorite samples, respectively. Compositions of bulk continental crust (BCC), lower continental crust (LCC), and upper continental crust (UCC) (Rudnick and Gao, 2003) are plotted for comparison. The explanation of Zr-Hf depletion in sample XKL12-19 is given in Fig. 12.

Fig. 12 (a) Zr vs. Hf diagram, showing good correlation, but sample XKL12-19 has the lowest Zr-Hf contents. (b) Zr vs. Lu diagram, showing sample XKL12-19 has the lowest HREE contents as represented by using Lu. (c) SiO_2 vs. Zr/Sm diagram, showing the effect of zircon crystallization for the granodiorite, reflected by rapid decrease of Zr/Sm with increasing SiO_2, but sample XKL12-19 deviates from the expected trend. (d) Y vs. Zr/Sm diagram, showing the decreasing heavy rare earth elements (represented by using Y) with decreasing Zr/Sm because of zircon crystallization. The best explanation for the obvious Zr-Hf depletion in sample XKL12-19 may be incomplete digestion of zircons rather than zircon crystallization.

Fig. 13 (a) Sr vs. SiO_2 and (b) Eu/Eu* vs. Sr diagrams, showing the effect of plagioclase fractionation for the dioritic dike and granodiorite samples, respectively.

Fig. 14 (a) and (b) $^{87}Sr/^{86}Sr_i$ and $\varepsilon_{Nd}(t)$ vs. SiO_2 diagrams for the dioritic dike and granodiorite samples, respectively. The data of dioritic dike samples show crustal

contamination although the trend is slight, but the data of granodiorite samples show a steeper trend which are more likely caused by magma mixing between mantle-derived melt and crustal melt.

Fig. 15 (a) Plots of $\varepsilon_{Nd}(t)$ vs. $^{87}Sr/^{86}Sr_i$ for the dioritic dike and granodiorite samples, a simple mixing model between depleted mantle (DM) ($^{87}Sr/^{86}Sr_i$ = 0.7030, $\varepsilon_{Nd}(t)$ = 9, Sr = 190 ppm, Nd = 19 ppm) (Zindler et al., 1984) and lower continental crust (LCC) ($^{87}Sr/^{86}Sr_i$ = 0.7010, $\varepsilon_{Nd}(t)$ = -28, Sr = 300 ~ 348 ppm, Nd = 11 ~ 38 ppm) (Liu et al., 2014; Rudnick and Gao, 2003) showing that the dioritic dikes are unlikely to originate from such mixing because of voluminous crustal material incorporation (~40% - 45%) required. (b) $^{87}Sr/^{86}Sr_i$ vs. 1/Sr showing an obvious linear trend for the dioritic dike samples, reflecting the AFC processes between enriched mantle (EM) ($^{87}Sr/^{86}Sr_i$ = 0.7050, Sr = 1027 ppm) and lower continental crust (LCC) ($^{87}Sr/^{86}Sr_i$ = 0.7010, Sr = 348 ppm) (Liu et al., 2014; Rudnick and Gao, 2003). A simple mixing line and two lines of presumed crustal contaminants are also plotted for comparison. D is the bulk partition coefficient for Sr, and r is the ratio between crustal assimilation rate and fractional crystallization rate. (c) $^{87}Sr/^{86}Sr_i$ vs. 1/Sr also showing an obvious linear trend for the granodiorite samples, and implying the mixing between mantle-derived melt and crustal melt.

Figure Supplementary

Fig. S1 (a-g) Analysis spots for other feldspar compositions of the dioritic dikes, (a) - (e): XKL12-25, (f): XKL12-26, (g): XKL12-27; and (h) melt corrosion/absorption with replacement by small grains of biotite and plagioclase in the clinopyroxene phenocryst (XKL12-21).

Fig. S2 Analysis spots for other feldspar compositions of the granodiorite, (a): XKL12-19, (b): XKL12-24, (c) - (e): XKL12-29.

Appendixes

Appendix 1 Sample locations and petrography of the Late Early Cretaceous granodiorite and dioritic dikes in the Hongqilafu pluton.

Appendix 2 Mineral major element compositions of the granodiorite and dioritic dikes in the Hongqilafu pluton.

Appendix 3 LA-ICP-MS zircon U-Pb data of the granodiorite and dioritic dikes in the Hongqilafu pluton.

Appendix 4 Whole-rock major and trace element data of the granodiorite and dioritic dikes in the Hongqilafu pluton.

Appendix 5 Whole-rock Sr-Nd-Hf isotopic compositions of the granodiorite and dioritic dikes in the Hongqilafu pluton.

Figure 1

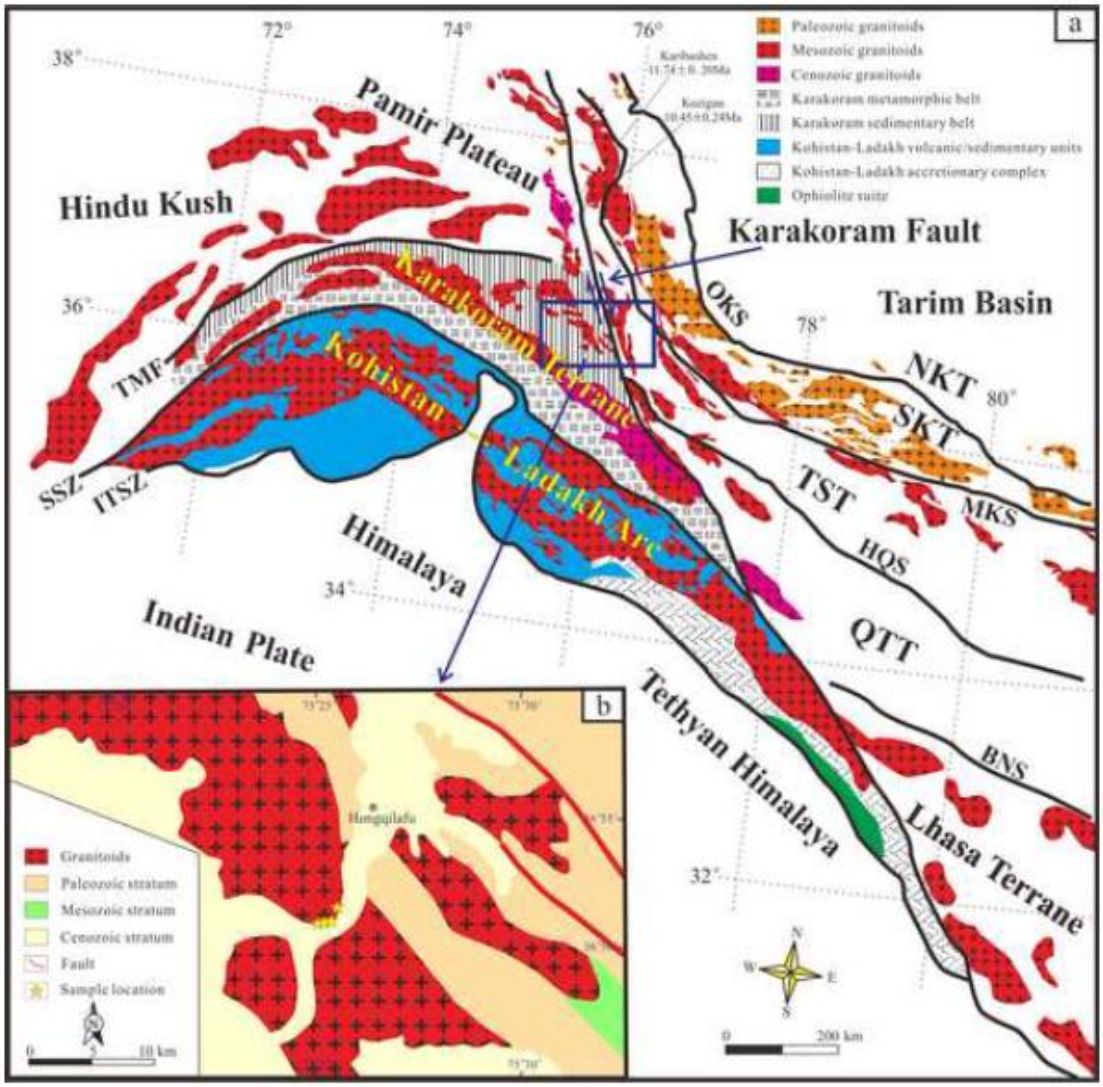

Figure 2

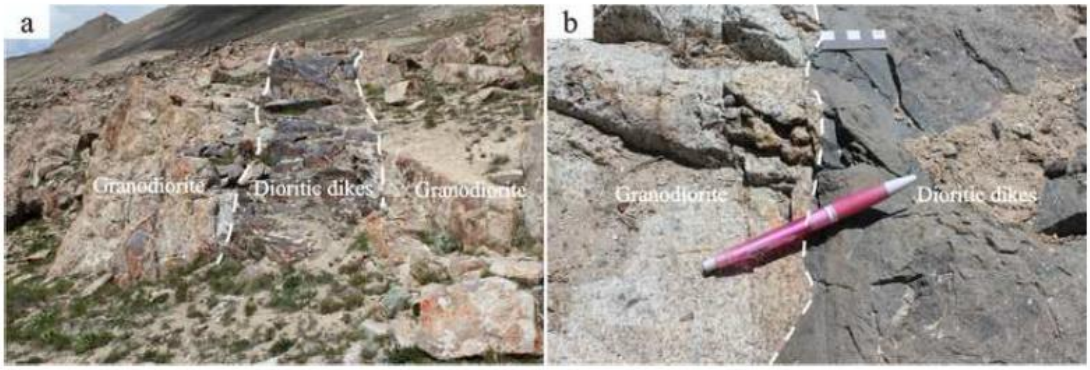

Figure 3

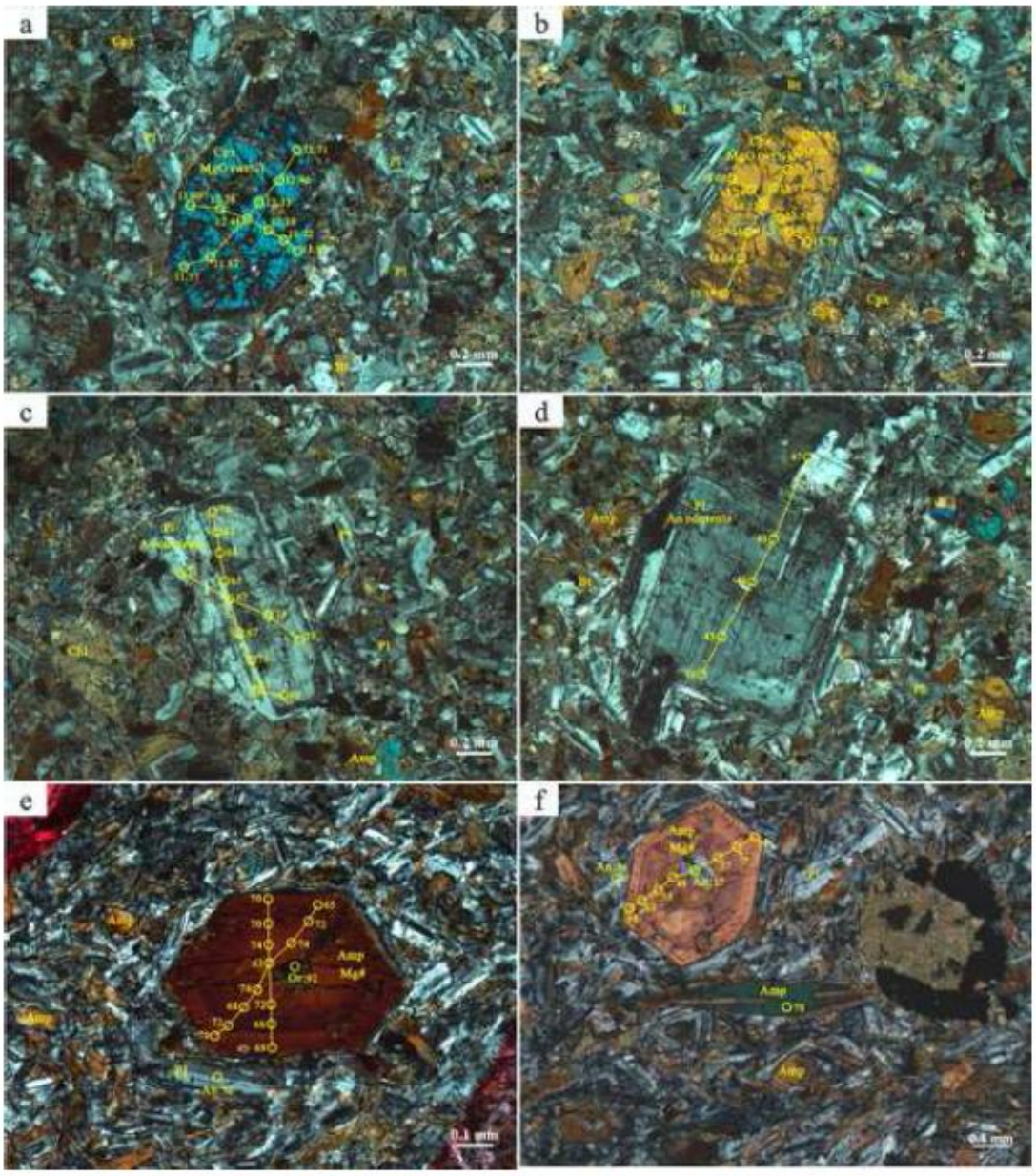

Figure 4

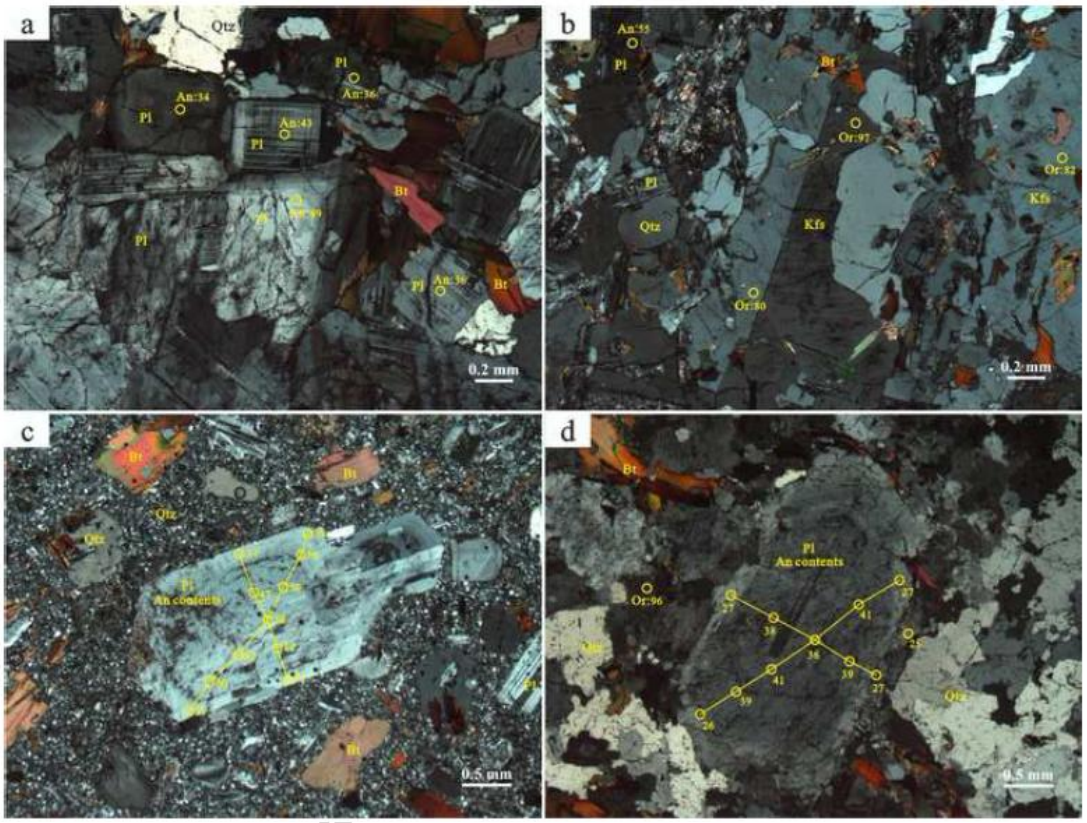

Figure 5

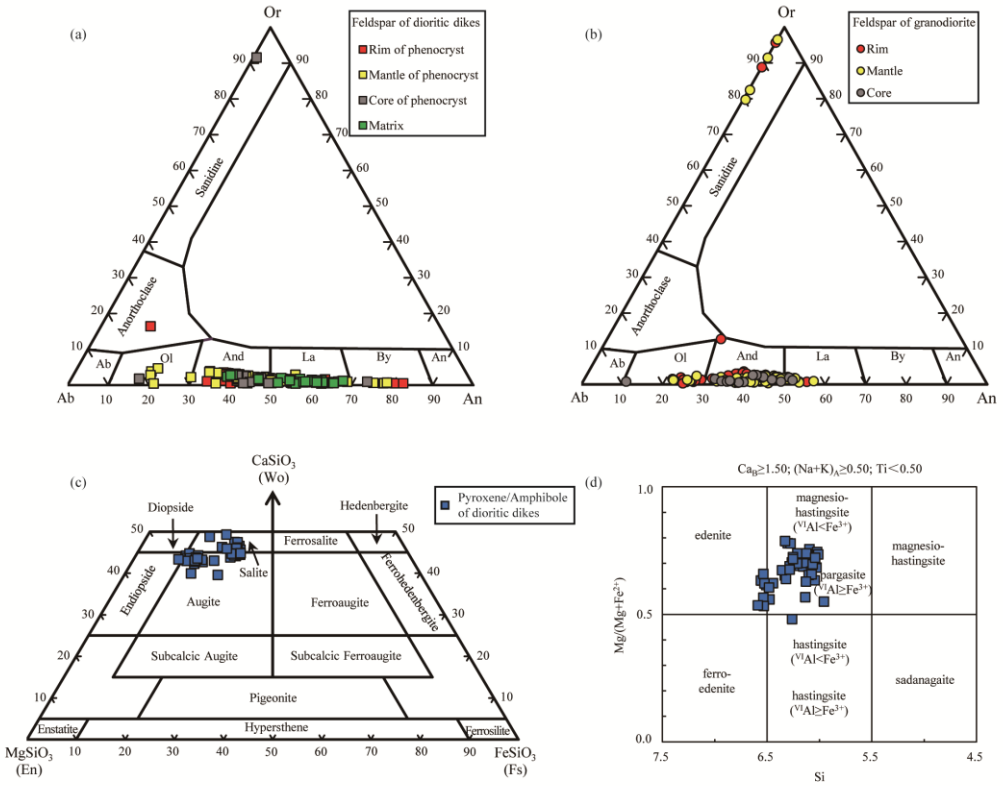

Figure 6

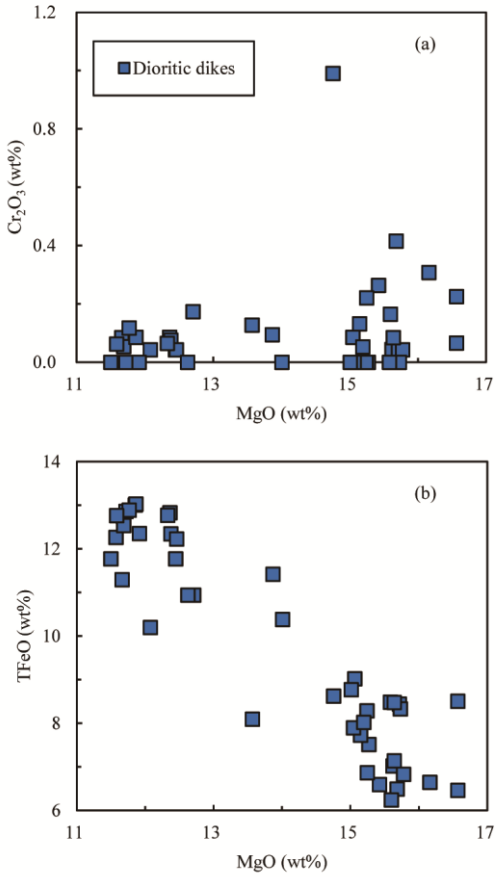

Figure 7

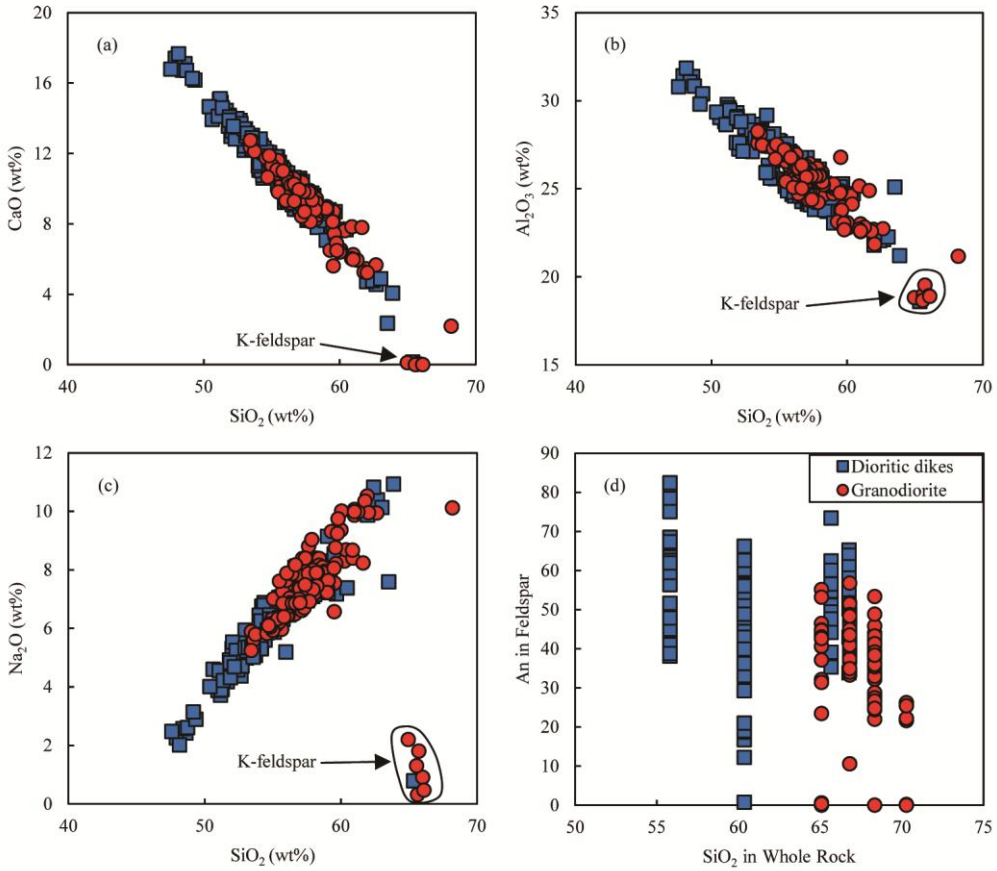

Figure 8

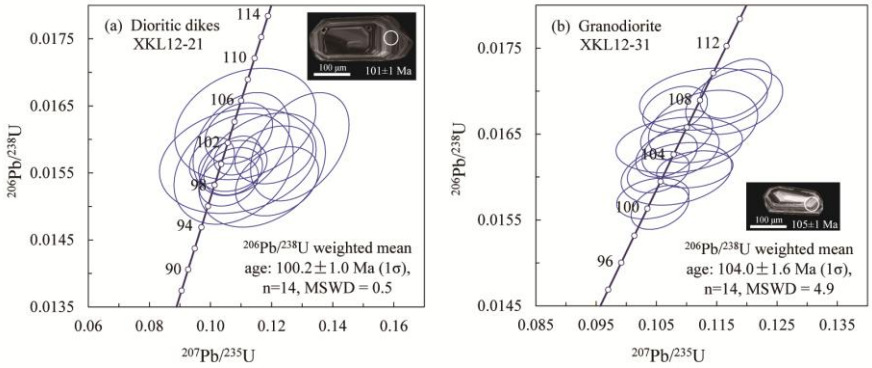

Figure 9

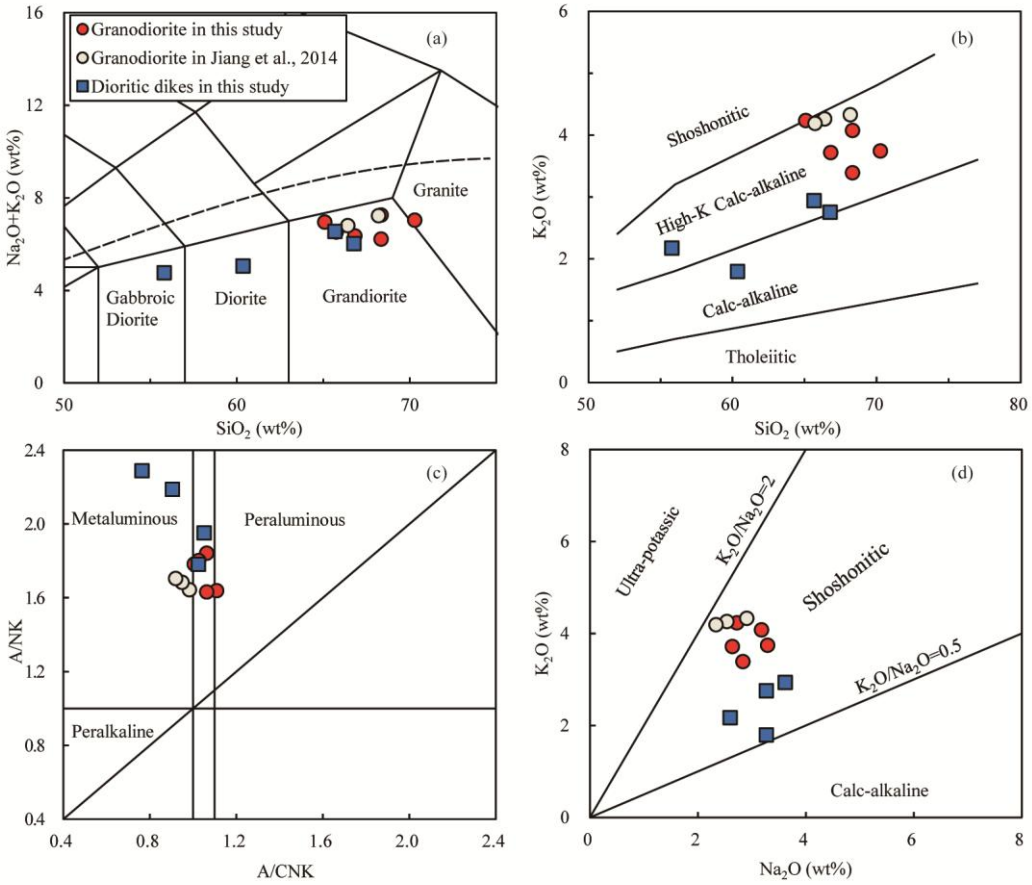

Figure 10

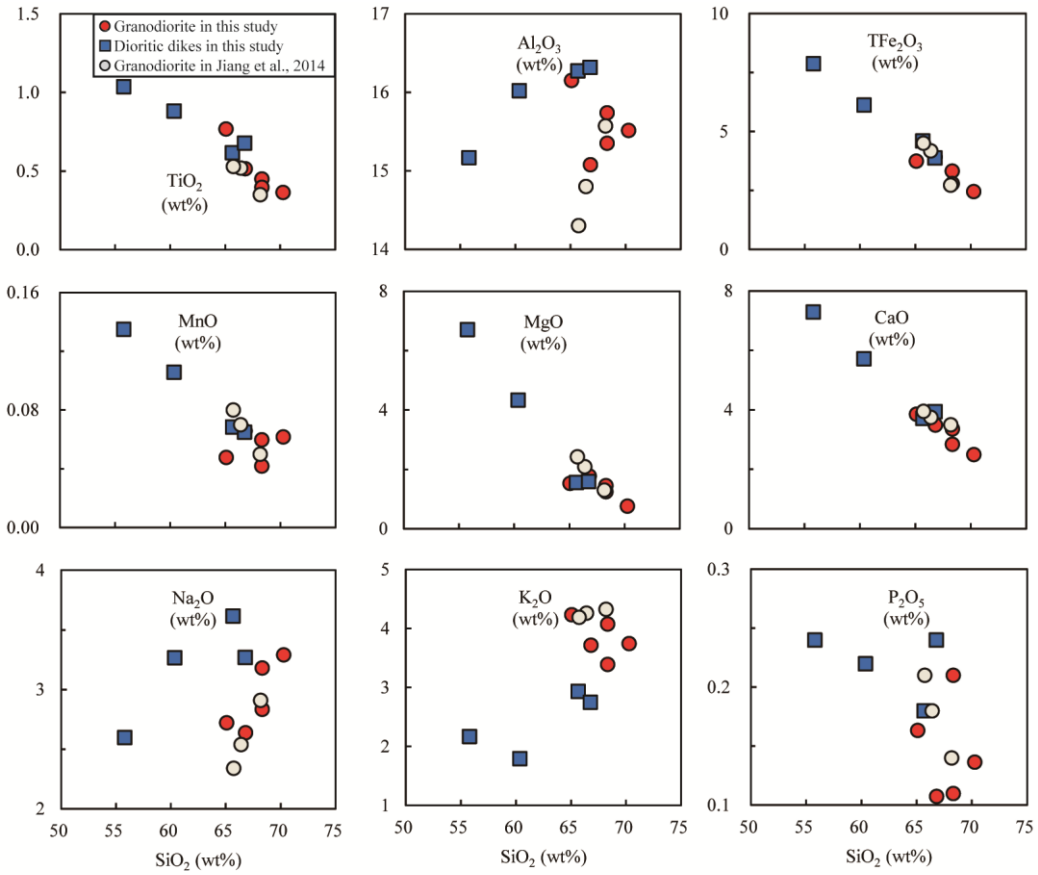

Figure 11

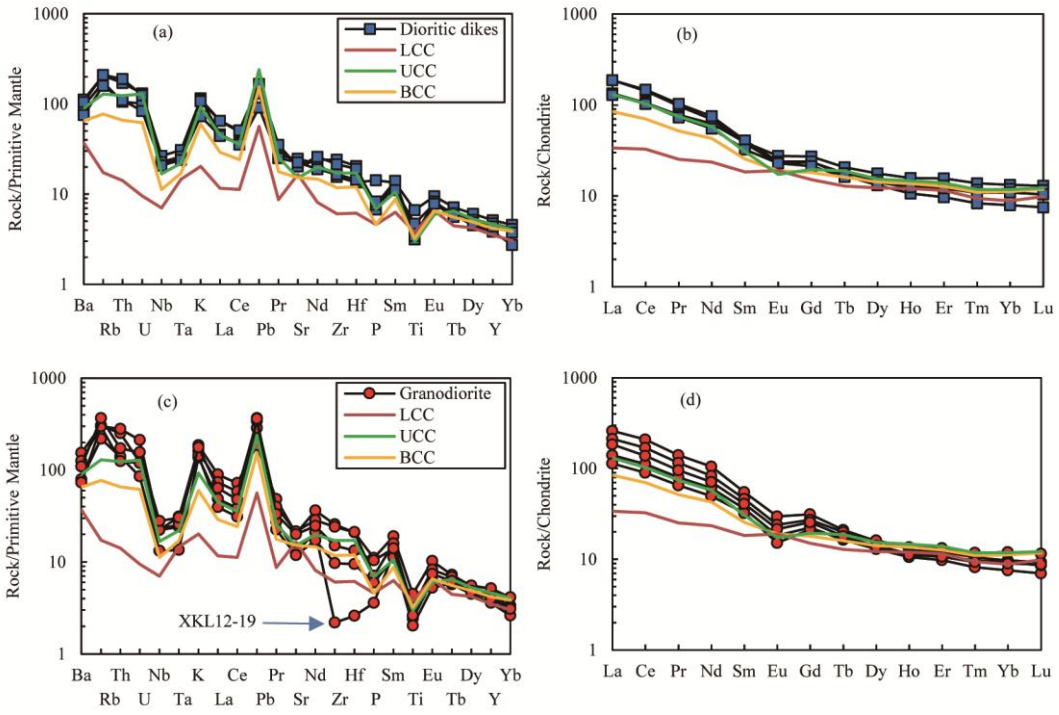

Figure 12

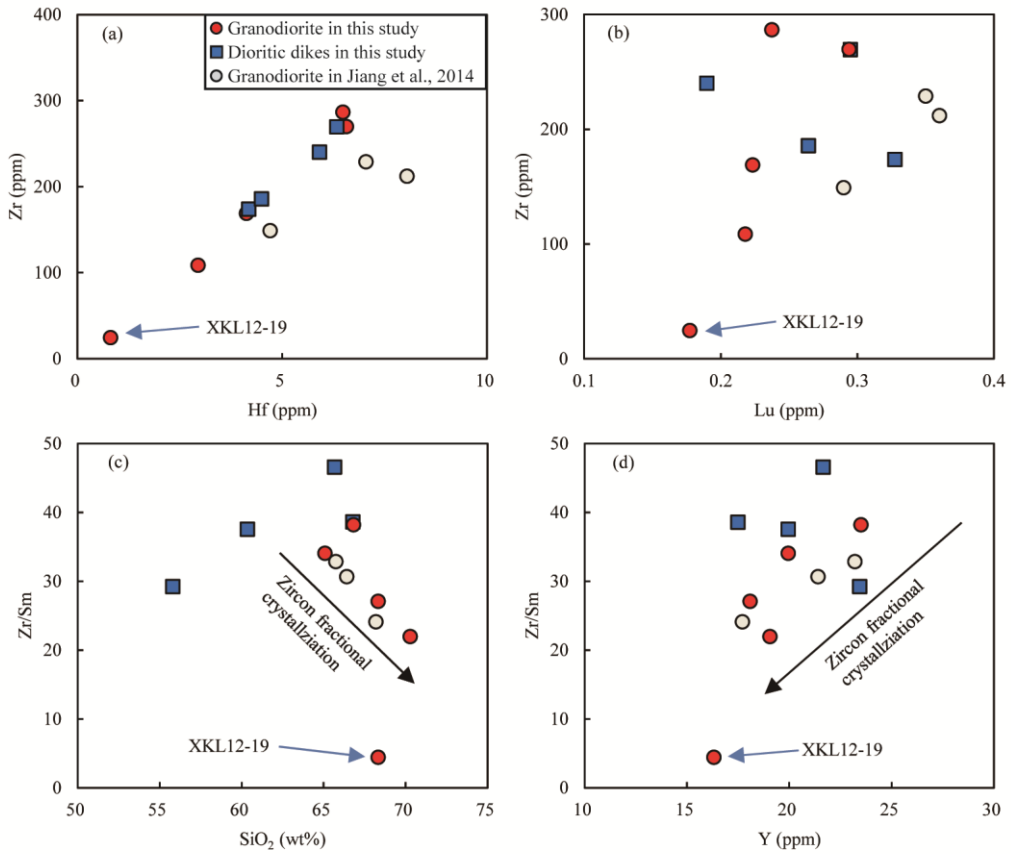

Figure 13

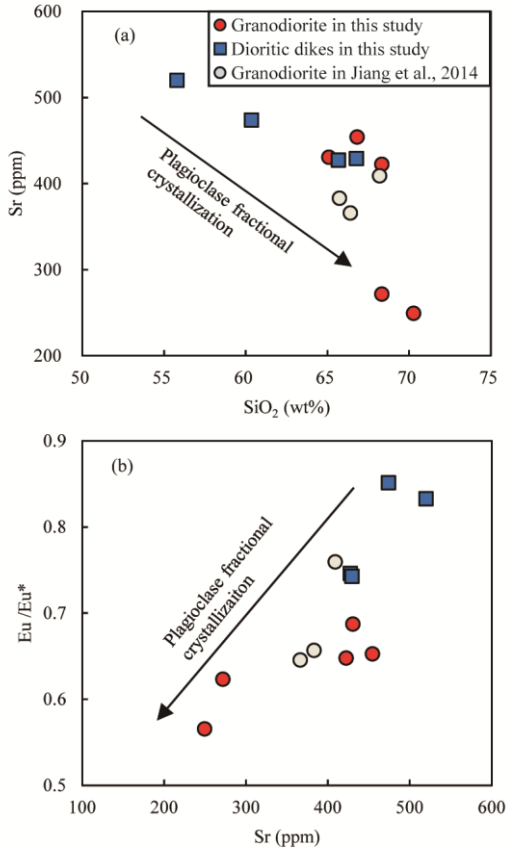

Figure 14

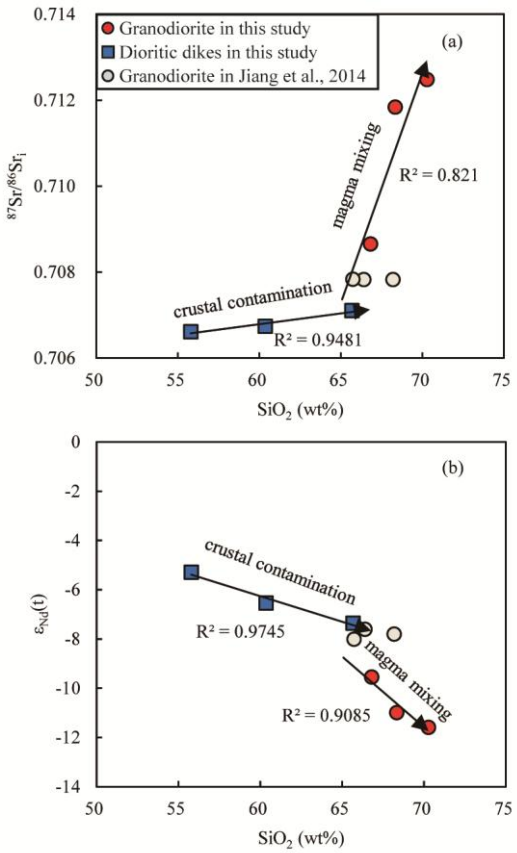

Figure 15

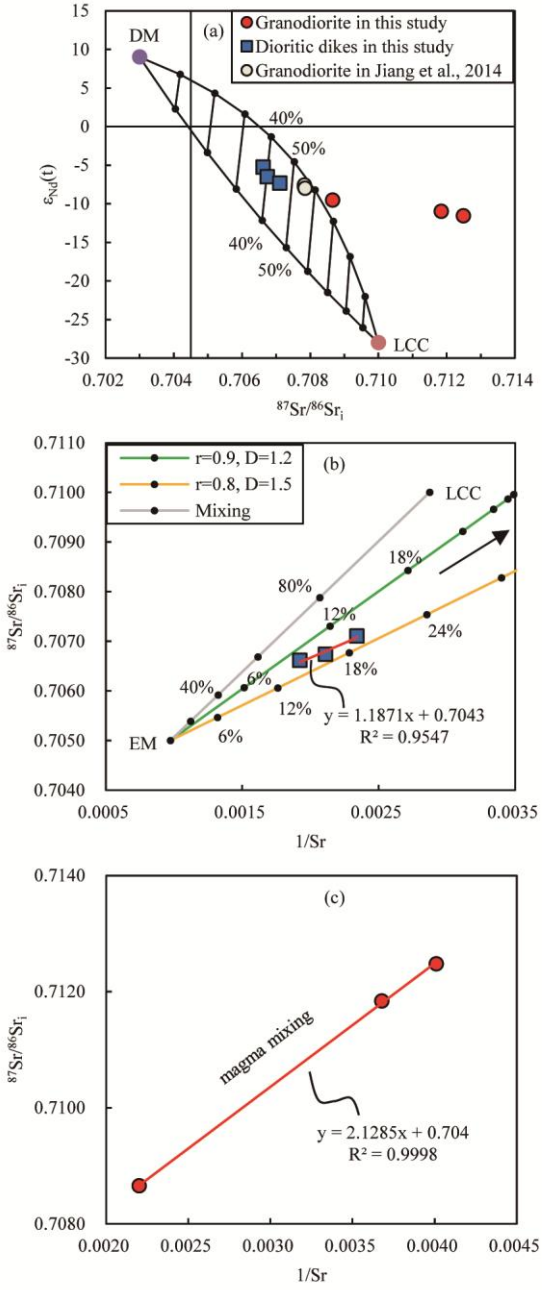

Highlights

1. The granodiorite and dioritic dikes in the Hongqilafu pluton are dated at ~104 Ma and ~100 Ma, respectively.

2. The dioritic dikes were generated by partial melting of metasomatized mantle wedge, followed by AFC processes.

3. The mantle-derived magma parental to the dioritic dikes underplated and induced the lower continental crust to melt, forming the granodiorite with mantle melt signatures.

4. The generation of the Hongqilafu pluton represents a large crust-mantle interaction event lasting for several million years at an active continental margin.